

Computational Fluid Dynamic Modeling of a Flame Reaction Process for Silica Nanopowder Synthesis from Tetraethylorthosilicate

Yanhui Ji,[‡] Hong Yong Sohn,^{†,‡} Hee Dong Jang,[§] Bin Wan,[‡] and Terry A. Ring[¶]

[‡]Department of Metallurgical Engineering, University of Utah, Salt Lake City, Utah 84112

[§]Nano-Materials Group, Korea Institute of Geoscience and Mineral Resources (KIGAM), Daejeon, Korea

[¶]Department of Chemical Engineering, University of Utah, Salt Lake City, Utah 84112

The process of synthesizing silica nanopowder by the gas phase thermal oxidation of tetraethylorthosilicate in a diffusion flame reactor was simulated using a commercial computational fluid dynamic code. The fuel combustion process and silica particle formation and growth in the flame were modeled. The temperature, velocity, and particle size distribution (PSD) fields inside the reactor were computed. Chemical reaction rate and a population balance model were used to calculate the particle formation and growth and PSD. Satisfactory results were obtained for the temperature profile and PSD. Computed values of the average size of the final products were consistent with those obtained in a previous experimental work.

I. Introduction

SILICA (SiO₂) nanoparticles are used as additives in plastics and rubbers to improve the mechanical properties of elastomers, and in a liquid system to improve the suspension behavior. The small size and therefore the high ratio of surface to volume of the particles is responsible for high catalytic activity; special optical properties; useful thermophysical, electric and, magnetic characteristics; and other properties such as flowability, plasticity, and toughness.^{1–3}

The most important and widespread use of silica nanoparticles in liquid systems is for the control and increase of viscosity and thixotropy. Thixotropy is the property of non-Newtonian pseudoplastic fluids to show a time-dependent change in viscosity; the longer the fluid undergoes shear, the lower its viscosity. Applications where silica nanopowder is used as a thickening or a thixotropic agent include adhesives, industrial chemicals, insecticides, lubricants, rubbers, and waxes.²

Silica nanopowder is also used as a suspending agent in many types of applications, such as aerosols, liquid coatings, inks, and pharmaceuticals. Silica nanopowder makes a very unique polishing suspension because it provides a chemical mechanical polishing (CMP) action for materials such as crystals, composites, and soft metals. At higher pH values (pH > 9.5), colloidal silica is held in nearly perfect suspension by the electrochemical repulsive forces of the fine particles themselves. Thus, it is faster and more reliable to remove both surface and subsurface damage on crystals, ceramics, and minerals by CMP with a colloidal silica slurry.

In dry systems, silica nanopowder acts as a dry lubricant, promoting free flow of the powder and preventing caking and lumping. The fumed silica layer decreases bulk tensile strength and shear strength of the powder, and its moisture-adsorbing ability helps it to perform an anticaking function. Owing to its ability to form network structures, silica nanopowder is used as a reinforcing agent in adhesives, sealants, rubber, and other elastomeric products. Silica nanopowder is also used to impart gloss reduction to materials used for protective or decorative coatings and to increase frictional resistance to slippage of surface coatings. Another important function is antiblocking. Antiblocking is a nonsticking property between two surfaces. Coatings with enhanced antiblocking ability have a good resistance to adhesion under the influence of temperature, relative humidity, or even pressure fusing the surfaces together. Plastic, rubber, and hot-melt adhesives tend to stick to each other when stored in close contact over time. Silica nanopowder imparts a small but effective roughness to the surface of any film in which it is embedded, preventing contact between the film and any other surface. In these and other applications, the particle morphology, average size, size distribution, and phase composition are the key characteristics of powders.²

The flame process has been used to produce various nanoparticles of ceramic and composite materials, ranging in size from a few to several hundred nanometers, because it provides a good control of particle size and crystal structure.^{4,5} This method can also produce high-purity particles continuously without further treatments such as drying, calcination, and milling. Silica nanoparticles are most commonly produced by the oxidation of silicon tetrachloride in a hydrogen–oxygen flame. Ulrich and Riehl,⁶ Zhu and Pratsinis,⁷ and Cho *et al.*⁸ studied the synthesis of silica nanoparticles in such a reaction system. Other precursors used include SiBr₄, hexamethyl disiloxane,⁹ and tetraethylorthosilicate (TEOS).^{10–14}

Although considerable work has been carried out on flame synthesis, the formation, growth, and distribution of particles in a flame with rapid temperature changes, chemical reactions, and complex fluid dynamics and mixing are still not well understood. In this work, mathematical modeling of the flame reaction process for the synthesis of silica powder from TEOS was performed. The goal was to simulate experimental results obtained by Jang, described in various papers.^{12–14} First, a commercial computational fluid dynamic (CFD) software package was adapted to the geometry and operating conditions of the flame reactor without including the particles, in order to obtain the correct temperature and velocity fields of the hydrogen–oxygen flame. The silica particle nucleation and growth was then incorporated into the simulation through the use of the nucleation kinetics and particle growth model, together with the population balance approach to keep track of the particle size distribution (PSD) at any point within the reactor.

S. Bhandarkar—contributing editor

Manuscript No. 23295. Received June 1, 2007; approved August 14, 2007.

This work was supported by the Korea Institute of Geoscience and Mineral Resources (KIGAM) and a Cooper-Hansen Fellowship awarded to Y. Ji from the College of Mines and Earth Sciences, University of Utah, during the course of this work.

[†]Author to whom correspondence should be addressed. e-mail: h.y.sohn@utah.edu

II. Modeling Approach

In the experimental work by Jang¹²⁻¹³ and Jang and Yoon,¹⁴ silica nanoparticles were synthesized by the gas phase thermal oxidation of TEOS in a laminar diffusion flame reactor. A modified burner composed of five concentric tubes was developed by Jang.¹² Silica nanoparticles ranging from 10 to 40 nm in average diameter were produced in the experiments.

The simulation of a flame reaction process involves the description of the fluid flow; heat and mass transfer processes; chemical reactions; and mixing of the gaseous components fuel, oxidant, and precursor as well as the particle formation and growth. The model resulting from such an approach is most realistic and, more importantly, can be used to predict with greater confidence the results of the process operated under various other sets of conditions.

A commercial computer software FLUENT (Lebanon, NH) was used as the main framework for the computation of the flame reaction process, by incorporating all the physical and chemical subprocesses described above.

(1) Reactor Configuration and Computational Mesh Generation

We created two-dimensional (2D) axisymmetric system meshes for the reactor used in the experiment by Jang.¹² A modified diffusion flame burner composed of five concentric tubes (2/10, 14/16, 18/22, 24/28, and 30/34 mm in ID/OD) was used in the experiments. A quartz tube 10 cm in diameter and 120 cm in length was installed outside the burner to contain the flame and particles. A schematic diagram of the experimental apparatus is shown in Fig. 1. Because of the axial symmetry of the reactor, only half of the domain is needed for simulation. Each inlet opening was divided by a minimum of four cell widths. The entire domain was 300 mm in length and 50 mm in radius. The number of cells in our successful runs for the hydrogen–oxygen flame simulation was 27 027. Figure 2 shows the details of the mesh design near the five raw material inlets of the modified diffusion flame burner composed of five concentric stainless tubes. Hydrogen (H₂) is used as the fuel while O₂ and air are used as the oxidants. Argon (Ar) gas saturated with TEOS vapor was introduced into the central tube of the burner.

This and the subsequent figures representing the reactor configuration show the vertical experimental reactor turned 90° clockwise. Thus, the bottom side represents the vertical centerline of the reactor. In some other figures, however, the

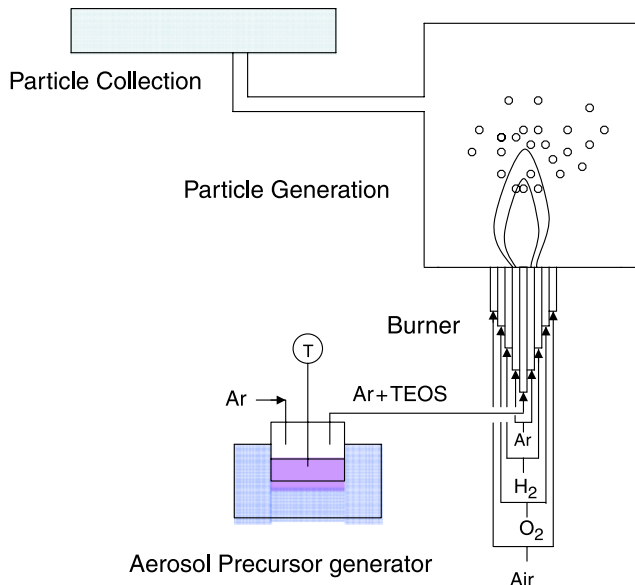


Fig. 1. Schematic diagram of experimental apparatus for the synthesis of silica nanoparticles.

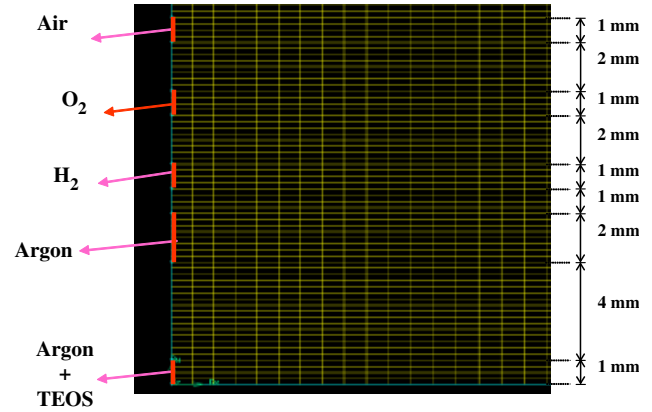


Fig. 2. Details of the mesh design near the five raw material inlets.

entire reactor is turned 90° clockwise, making the bottom the opposite wall. The left side of the figure represents the bottom of the reactor with five concentric openings for raw material injection. The top of the figure represents the reactor wall and the right side represents the top of the reactor where the gas and particles leave the reactor. The nearer to the centerline and the inlet, the denser the meshes.

(2) CFD Process

(A) *Basic Governing Equations*¹⁵: The following partial differential equations are solved to compute velocity, temperature, pressure, and species concentration fields inside the reactor. These equations were solved using a finite control volume approach by means of the axisymmetric 2D solver available within the FLUENT software. In our model, the dependent variables stand for the mixture of a gas and solid phase in the following equations, which assumes the same temperature for the particles and the surrounding gas in a cell.

(1) *Continuity equation*:

$$\nabla \cdot (\rho \vec{v}) = 0 \quad (1)$$

(2) *Momentum conservation equations*:

$$\nabla \cdot (\rho \vec{v} \vec{v}) = -\nabla p + \nabla \cdot (\bar{\tau}_+ + \bar{\tau}_t) \quad (2)$$

where p is the static pressure, $\bar{\tau}$ is the stress tensor and is given by

$$\bar{\tau} = \mu[(\nabla \vec{v} + \nabla \vec{v}^T) - \frac{2}{3} \nabla \cdot \vec{v} I] \quad (3)$$

where μ is the molecular viscosity, I is the unit tensor, and the second term on the right-hand side is the effect of volume dilation.

(3) *Turbulence equations*: The turbulence kinetic energy κ and the specific dissipation rate ε are obtained from the following transport equations:

$$\frac{\partial}{\partial t} (\rho \kappa) + \frac{\partial}{\partial x_i} (\rho \kappa u_i) = \frac{\partial}{\partial x_j} \left(\Gamma_\kappa \frac{\partial \kappa}{\partial x_j} \right) + G_\kappa - Y_\kappa + S_\kappa \quad (4)$$

and

$$\frac{\partial}{\partial t} (\rho \varepsilon) + \frac{\partial}{\partial x_i} (\rho \varepsilon u_i) = \frac{\partial}{\partial x_j} \left(\Gamma_\varepsilon \frac{\partial \varepsilon}{\partial x_j} \right) + G_\varepsilon - Y_\varepsilon + S_\varepsilon \quad (5)$$

where G_κ is the generation of turbulence kinetics energy due to mean velocity gradients. G_ε is the generation of ε . Γ_κ and Γ_ε represent the effective diffusivity of κ and ε , respectively. Y_κ and Y_ε represent the dissipation of κ and ε due to turbulence. S_κ and S_ε are the user-defined source terms.

(4) Energy equations:

$$\rho C_p (\vec{v} \cdot \nabla T) = k \nabla^2 T + \sum_{i=1}^n h_i M_i \omega_i \quad (6)$$

where C_p is the heat capacity, T is the temperature, and k is the conductivity coefficient. h_i is the enthalpy of species i , M_i is the molecular weight of species i , and ω_i is the net production of species i by a homogeneous chemical reaction.

(5) Species transport equations:

$$\nabla \cdot (\rho \vec{v} Y_i) = -\nabla \cdot \vec{J}_i + R_i + S_i \quad (7)$$

where R_i is the net rate of production of species i by a chemical reaction and S_i is the rate of creation by addition from the dispersed phase plus any user-defined sources. Y_i is the mass fraction of each species. J_i is the diffusion flux of species i , which arises due to concentration gradients.

(6) Equation of state:

$$p = (\rho / M_w) RT \quad (8)$$

(7) The population balance equation¹⁶:

$$\frac{\partial}{\partial L} (nG) + \nabla \cdot (n\vec{v}) = \text{Birth} - \text{Death} \quad (9)$$

where n is the particle number density function, L represents the particle size (particle diameter), G is the growth rate of the particles, and \vec{v} is the gas-phase velocity vector. The birth and death source terms represent the rates of particles birth and death due to breakage, aggregation, and other related phenomena.

The boundary condition^{15,16} at $L = 0$ for the integration of the second term of Eq. (9) is obtained from

$$n \cdot dL|_{L=0} = J \cdot \Delta t = J \left(\frac{dL}{G} \right) \quad (10)$$

and thus

$$n(0, t) \cdot G = J \quad (11)$$

where J represents the rate of nucleation of particles.

(B) *Materials and Operating and Boundary Conditions:* The eight species considered in the simulation are H₂, O₂, H₂O, N₂, CO₂, Si(OC₂H₅)₄ (TEOS), SiO₂, and Ar. The total pressure was 1 atm (101.3 kPa), and the inlet mass fraction for each species was specified. At the walls, zero-gradient (zero-flux) boundary conditions were applied for all species (standard wall function) and the temperature was maintained at 298 K.

We start with the initial values for temperature at 2000 K, O₂ mass fraction of 0.23, H₂ mass fraction of 0.1, and Si(OC₂H₅)₄ mass fraction of 10⁻⁸. The residues for continuity, component velocities, and energy are set at 10⁻⁶ as the convergence criteria; the residues of six moments (moments 0–5) are set at 10⁻⁴; and all the others at 10⁻³. These are the default criteria recommended by FLUENT. For the system simulated in this work, the convergence criterion for energy is usually met last and thus residues for other variables are several orders of magnitude smaller than the above-set values by the time convergence is declared.

(3) Combustion and Chemical Reactions

The species transport and finite-rate chemistry modeling, which is one of the five combustion modeling approaches in FLUENT, was chosen for this work. The reaction rates that appear as source terms are computed by the combined finite-rate/eddy-dissipation model.

Most fuels are fast burning, and the overall rate of reaction is controlled by turbulent mixing. Thus, the complex and often unknown chemical kinetic rates can be safely neglected. However, it is often useful to incorporate the slower chemical kinetic rate to act as a “switch,” preventing reaction in a region of low temperature where ignition may not have occurred. In such a case, the Arrhenius rate parameters may not have to be exact. Once the flame is ignited, the eddy-dissipation rate is generally smaller than the Arrhenius rate, and reactions are mixing limited.

For a laminar finite-rate model, the rate is represented by the Arrhenius expression:

$$k_f = A_r T^{\beta_r} \exp(-E_r/RT) \quad (12)$$

where A_r is the preexponential factor (consistent units); β_r is the temperature exponent (dimensionless); E_r is the activation energy for the reaction (J/kmol); and R is the universal gas constant (J · kmol⁻¹ · K⁻¹).

For the eddy-dissipation model, reaction rates are assumed to be controlled by the turbulence, which is correct when chemical kinetics are fast, and thus extensive Arrhenius chemical kinetic calculations can be avoided. The net rate of production of species i due to reaction, R_{ir} , is given by the smaller (that is, the limiting value) of the two expressions below¹⁷:

$$R_{ir} = v_{ir} M_{wi} A \rho \frac{\varepsilon}{k} \min \left(\frac{Y_R}{v_{Rr} M_{wR}} \right) \quad (13)$$

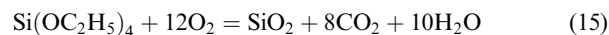
$$R_{ir} = v_{ir} M_{wi} A B \rho \frac{\varepsilon}{k} \frac{\sum_P Y_P}{\sum_j^N v_{jr} M_{wj}} \quad (14)$$

where v_{ir} is the stoichiometry coefficient for reactant i in reaction r , v_{jr} is the stoichiometry coefficient for product j in reaction r , M_{wi} is the molecular weight of species i , and ρ is the density. Y_P is the mass fraction of any product species, P ; Y_R is the mass fraction of a particular reactant, R ; A is an empirical constant equal to 4; and B is an empirical constant equal to 0.5.

In this work, the combined finite-rate/eddy-dissipation model is used, where both the Arrhenius and the eddy-dissipation reaction rates are calculated. The net reaction rate is taken as the minimum of these two rates.

For the combustion of hydrogen (H₂+1/2O₂=H₂O), the preexponential factor A_r is 9.87 × 10⁸, the activation energy E_r is 3.1 × 10⁷ J/kmol, and the temperature exponent β_r is zero. The FLUENT calculates the Arrhenius rate by $R_A = A_r T^{\beta_r} \exp(-E_r/RT) C_{H_2} C_{O_2}$ (kmol · (m³ · s)⁻¹), and also calculates the eddy-dissipation reaction rate by above Eqs. (13) and (14). Then, the net reaction rate is taken as the minimum of these rates.

The computation started by forming the flame based on the reaction of H₂ and O₂. For this purpose, the TEOS and Ar inlet stream was replaced by pure Ar. When the result is converged, we added the oxidation reaction of TEOS:



For the oxidation of TEOS, we used the oxidation kinetics of tetramethyl-silane [Si(CH₃)₄] from the databank in FLUENT, due to the lack of data for TEOS. However, we retained the chemical formula and the molecular weight of TEOS. Thus, the preexponential factor used was 10¹⁵, the activation energy was 10⁸ J/kmol, and the temperature exponent was zero. The eddy-dissipation reaction rate was also calculated by the above Eqs. (13) and (14). Then, the net reaction rate was taken as the minimum of these rates.

We mixed TEOS in an Ar carrier gas in the TEOS input stream through the innermost feed tube. Because of the small amount of TEOS added, the results for the profiles of temperature, mass density, and concentrations of hydrogen, oxygen, water vapor, nitrogen, and Ar remain essentially unchanged.

However, this further gives us confidence that we can add other gas-phase reactions and the numerical simulation will still remain stable. The concentrations of the products, silica and carbon dioxide, of the oxidation of TEOS were obtained and shown below.

(4) Particle Formation and Growth

The determination of the nucleation and growth kinetics for silica from the oxidation of TEOS is an extremely difficult problem, despite considerable research on the subject.^{6,18} Greatly simplified expressions were used in this work for these rates, together with assumed values of the rate parameters. Thus, we treated these kinetic parameters as adjustable parameters and determined the best set of values by comparing the results with available experimental data for the particle size of silica powder obtained by the flame synthesis.

Assuming power-law kinetics for the nucleation rate, the nucleation rate was expressed by

$$J = k_n(S - 1)^{N_n} \quad (16)$$

where J ($\# \cdot s^{-1} \cdot m^{-3}$) is the nucleation rate, k_n ($\# \cdot s^{-1} \cdot m^3$) represents the rate constant, and the exponent N_n was assumed to be 1. S is the degree of supersaturation (equals to p_{SiO_2}/p_{SiO_2} at saturation). In this work, J was set equal to zero when $S < 1$. This is equivalent to not volatilizing solid silica once it is formed.

The results for the size-distribution characteristics of the silica particles produced by the oxidation of TEOS in a flame reaction process are expressed in terms of the appropriate moments of the size distribution. The i th moment m_i is defined by¹⁶

$$m_i = \int_0^\infty L^i n(L) dL \quad (17)$$

where $L(m)$ is the particle size, and $n(L)$ is the particle number density function. The zeroth moment represents the total number of particles per unit volume. The first moment represents the total length of particles per unit volume. The second moment represents the total surface area of particles per unit volume. The third moment represents the total volume of particles per unit volume.¹⁹ The final PSD is obtained by solving the population balance equation using the standard method of moments or the quadrature method of moments (QMOM).^{16,20,21}

The linear growth rate of a particle under the control of mass transfer is given by

$$G_m = 4V_{mol}D_{AB} \frac{1.013 \times 10^5}{8.314T} Y_{SiO_2}^* (S - 1) \frac{m_0}{m_1} \quad (18)$$

where V_{mol} is the molar volume of the silica particle (m^3/mol); D_{AB} (m^2/s) is the diffusion coefficient, which is a function of temperature (in this work, A is SiO_2 ; B is O_2 , which is the predominant gas species); S is the degree of supersaturation (equal to p_{SiO_2}/p_{SiO_2} at saturation); m_0 is the zeroth moment ($1/m^3$) of the PSD; m_1 is the first moment (m/m^3) (thus, m_1/m_0 represents the number-averaged particle size); $Y_{SiO_2}^*$ is the mole fraction of SiO_2 at saturation; and T is the temperature (K).

The growth rate under the control of chemical reaction kinetics G_c (m/s) was assumed to follow the following expression:

$$G_c = k_g(S - 1)^{N_g} \quad (19)$$

where k_g (m/s) represents the rate constant, and the exponent N_g was assumed to be 1.

The total growth rate G under the combined control of mass transfer and chemical reaction kinetics can then be calculated by

$$G = \frac{G_c G_m}{G_c + G_m} \quad (20)$$

In this work, G was set equal to zero when $S \leq 1$. This is again equivalent to not volatilizing solid silica once it is formed.

In the system studied in this work, the growth rate under the control of chemical reaction kinetics was the limiting factor. This means that the growth rate under the control of mass transfer is much faster than the growth rate of chemical reaction kinetics.

In terms of the particle growth rate, the rate of increase of the solid mass per unit volume of the system in mass balance is given by

$$\text{Source} = (\pi/2)m_2 G \rho \quad (21)$$

where ρ is the solid density (kg/m^3) and m_2 is the second moment of the PSD (m^2/m^3), which represents the total surface area of particles per unit volume of the reactor.

III. Results and Discussion

(1) Temperature and Velocity Profiles

Figure 3 shows the converged result for temperature contour, which indicates that the computed temperature field is very realistic in terms of the magnitude and distribution. It is highest where the main fuel hydrogen comes in contact with oxygen and decreased in the axial and radial directions, enveloping a region reasonably shaped like a flame.

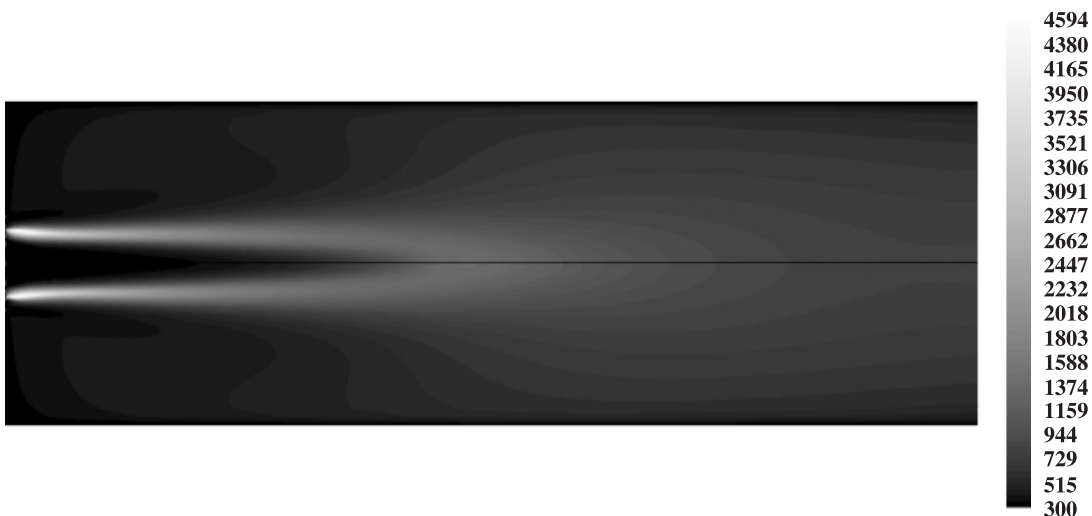


Fig. 3. Contours of temperature (K).

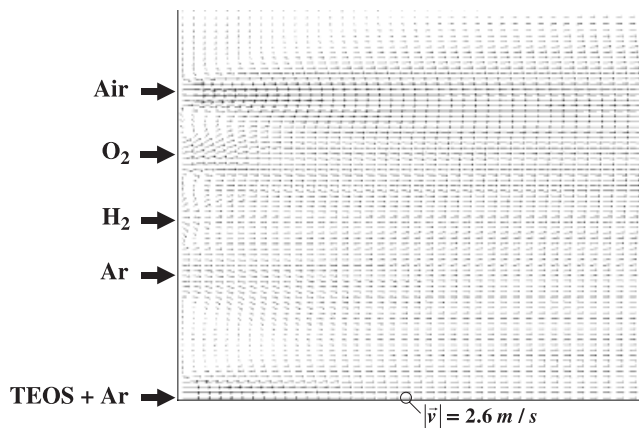


Fig. 4. Contours of velocity magnitude (m/s).

The distribution of the velocity magnitude, shown in Fig. 4, is reasonable in both axial and radial directions. The converged result gave us confidence that the simulation was correct as far as the velocity as a function of position was concerned.

The contours of the stream function (the iso-stream function lines), shown in Fig. 5, represent the paths of the fluid elements. Further, the magnitude of the stream function indicates the flow rate between two adjacent lines. It is seen that the radial expansion of the gas flow is simulated correctly and the magnitude of the flow rate is reasonable. In addition, the presence of a recirculating zone is indicated correctly. This converged result adds to our confidence for the computation of the velocity field under the experimental conditions to be simulated.

The solution was converged after some 20 000 iterations. Most residuals are under 10^{-6} , with a few being below 10^{-5} . It took more than 10 h of computation on a computer with a Pentium 4.3 GHz processor and 1 GB memory.

(2) PSD and Discussion

The nucleation rate and growth rate are two important factors that determine the particle size. Table I summarizes the computed PSD parameters with various combinations of the nucleation rate constant k_n and the particle growth rate constant k_g in Eqs. (16) and (19), respectively. Because there are no independently measured data on these parameters for the system being simulated, we adopted the approach to perform a parametric study to investigate the effect of these parameters on the PSD of the final product powder. These results were obtained by QMOM and the mean particle sizes were calculated by the area-weighted average diameter. Experimentally, the average particle diameter L_a was obtained from the measured specific surface area A and particle density ρ_p .¹² Thus, L_a is calculated from the computed results by

$$L_a = \frac{6}{\rho_p A} = \frac{6}{\rho_p \frac{S}{\rho_p V}} = \frac{6V}{S} = \frac{6 \int_0^\infty L^3 n(L) dL}{\pi \int_0^\infty L^2 n(L) dL} = \frac{m_3}{m_2} \quad (22)$$

where L_a is the average particle diameter, S is the surface area of the particles, V is the volume of the particles, m_2 and m_3 are the

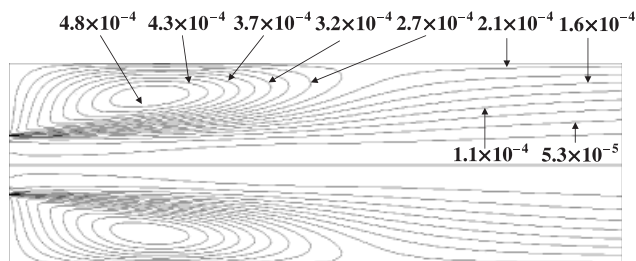


Fig. 5. Contours of stream function (kg/s).

Table I. Particle Size Distribution of Product Powder with Different Nucleation Rate and Growth Rate Constants

k_n (#/s)	k_g (m/s)	Average particle diameter based on specific surface	
		area (m_3/m_2) (nm)	$cv = [m_4 \times m_2 / (m_3)^2 - 1]^{1/2}$
1×10^{-2}	1×10^{-26}	10	0.55
1×10^{-2}	1×10^{-25}	61.4	0.59
1×10^{-1}	1×10^{-25}	36.7	0.61
1	1×10^{-26}	8.75	0.56
1	1×10^{-25}	20.9	0.63
1	1×10^{-24}	40.1	0.73
10	1×10^{-25}	11.9	0.67
10	1×10^{-24}	22.6	0.71
10	1×10^{-23}	36.8	0.52
10	1×10^{-22}	57.2	0.45
1×10^2	1×10^{-25}	7	0.72
1×10^2	1×10^{-24}	12.5	0.65
1×10^2	1×10^{-23}	19.7	0.48
1×10^3	1×10^{-26}	2.1	0.63
1×10^3	1×10^{-25}	4	0.73
1×10^3	1×10^{-24}	6.8	0.59
1×10^3	1×10^{-22}	17.3	0.44
1×10^4	1×10^{-25}	2.3	0.71
1×10^4	1×10^{-24}	3.7	0.52
1×10^4	1×10^{-23}	5.7	0.45

Product particle size distribution (experimental reactor used by Jang¹²): O₂, 15 L/min; Air, 40 L/min; H₂, 6 L/min; Ar, 10 L/min; carrier gas (Ar), 1 L/min. $G = G_c \times G_m / (G_c + G_m)$, where G is the total growth rate; $G_c = k_g \times (S - 1)^{N_g} (\text{m} \cdot (\text{m}^3 \cdot \text{s})^{-1})$. G_m , growth rate by mass transfer. $J = k_n \times (S - 1)^{N_n} (\# \cdot (\text{m}^3 \cdot \text{s})^{-1})$; Nucleation rate. TEOS concentration is 0.6% (4.73×10^{-5} mol/L). TEOS, tetraethylorthosilicate.

second and third moments, respectively, and $n(L)$ is the number density function.

From Table I, it can be seen that a 10-fold increase in the nucleation rate constant k_n for the same growth rate constant results in a decrease of the particle diameter by approximately half. This agrees with the fact that when the nucleation rate increases by 10 times, approximately 10 times more particles form, and the average particle volume reduces to one-tenth. Thus, the particle diameter decreases to the cubic root of one-tenth, that is, $1/2.15$, which is about half the original diameter.

The coefficient of variation, cv , represents the degree of spread of the size distribution, defined as the ratio of the standard deviation of a distribution to its mean size. The particle size used here is the average particle diameter based on specific surface area, as described in Eq. (22). Then, the coefficient of

Table II. Average Particle Diameter of the Product Powder for the Best Set of Combinations of the Nucleation and Growth Rate Constants

k_n (#/s)	k_g (m/s)	Computed average particle diameter based on specific surface area (m_3/m_2) (nm)	
		TEOS (2.5×10^{-4} mol/L)	TEOS (9.8×10^{-6} mol/L)
20	2×10^{-24}	31.2	15.3
15	10^{-24}	29.2	13.5
10	10^{-24}	32.5	14.8
10	10^{-23}	51.9	26.8
8	10^{-24}	34.5	15.6

Particle size 11 nm—(TEOS 9.8×10^{-6} mol/L = 0.12 wt%) (experiment by Jang¹²). Particle size 38 nm—(TEOS 2.5×10^{-4} mol/L = 3.1 wt%) (experiment by Jang¹²). Product particle size comparison (experimental reactor used by Jang¹²). O₂, 15 L/min; Air, 40 L/min; H₂, 6 L/min; Ar, 10 L/min; carrier gas (Ar), 1 L/min. TEOS, tetraethylorthosilicate. Boldface signifies that this combination of k_n and k_g gave the best results.

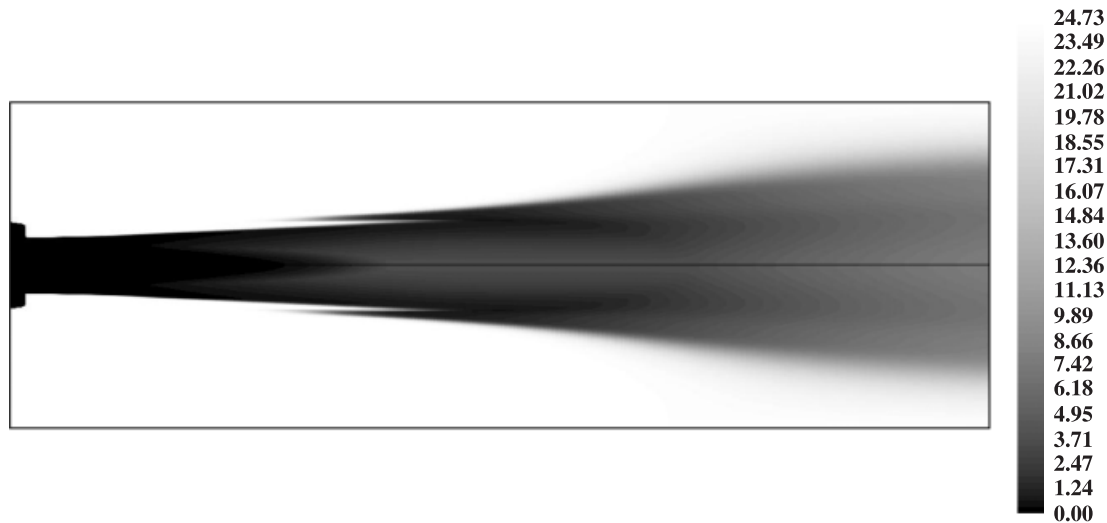


Fig. 6. Contours of volume average particle diameter (m) ($k_n = 8 \text{ \#}/s$, $k_g = 10^{-24} \text{ m}/s$, $\text{TEOS} = 9.8 \times 10^{-6} \text{ mol}/L$). TEOS, tetraethylorthosilicate.

variation is given in terms of the moments as follows:

$$cv = \sqrt{\frac{m_4 m_2}{(m_3)^2} - 1} \tag{23}$$

In Jang’s study,¹² the effects of key variables such as precursor (TEOS) concentration, total gas flow rate, and gas composition in the diffusion flame from the burner on the particle size were investigated. According to the experiments by Jang,¹² as the TEOS concentration in the flame was increased from 9.8×10^{-6} to $2.5 \times 10^{-4} \text{ mol}/L$, the average diameter based on specific surface area (m_3/m_2) increased from about 11 nm to about 38 nm. Various combinations of the nucleation and growth rate constants were tested, and some typical results are shown in Table II. The combination of the rate constants $k_n = 8 \text{ \#}/s$ and $k_g = 10^{-24} \text{ m}/s$ used in the simulation resulted in the corresponding diameters of 15.6 and 34.5 nm. Because there are other uncertainties in both the experiments and simulation in terms of measurements in the former and rate expressions in the latter, closer matching between the experimental and simulation results would not be meaningful. Thus, this combination of rate constants was used to simulate experiments performed under other conditions. Figures 6 and 7 show typical examples of the PSD computed with these values. These figures show the average particle diameter inside the reactor at any point. From these

figures, we see that the average particle size is small close to the centerline and larger close to the wall. The reason is because the particle remains longer near the wall.

Table III shows the comparison of product particle size between the experiment and the simulation. The first two cases in this table are those used to determine the best combination of the rate constants, as shown in Table II. Case 3 shows that when the TEOS concentration was changed to $1.91 \times 10^{-4} \text{ mol}/L$ and the airflow rate were changed to 20 L/min, the experimental particle diameter was 26 nm. The computer simulation of this run resulted in a reasonably close average diameter of 30.8 nm.

Cases 4–9 were tested for the effect of gas composition in the burner on the average particle size of the product.

As the first change, Ar gas in the second tube of the burner was replaced with air. By comparing cases 1 and 4, it can be seen that this change results in an increase in the particle size due to the higher oxygen concentration and the resulting lower degree of dilution of the silica vapor. The computed increase was considerably smaller than the experimentally observed one. The effect of TEOS concentration on the product particle size can be seen by comparing cases 4 and 5. As the TEOS concentration increased from 9.8×10^{-6} to $1.88 \times 10^{-4} \text{ mol}/L$, the average diameter of silica particles increased from 21 to 32 nm.

As the second change, the oxygen flow rate in the fourth tube of the burner was decreased from 15 to 5 L/min while air (10 L/min) was injected through the second tube and the total

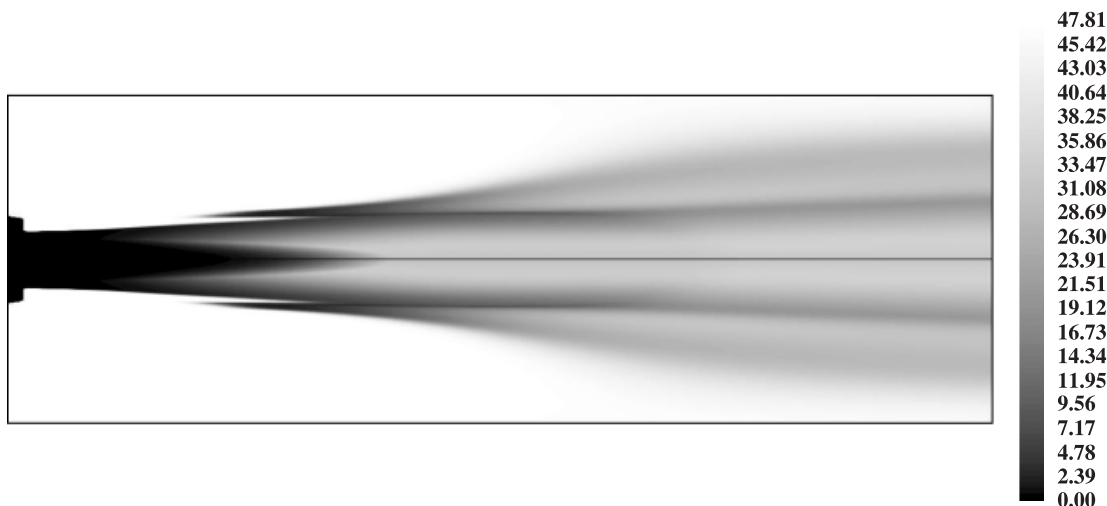


Fig. 7. Contours of volume average particle diameter (m) ($k_n = 8 \text{ \#}/s$, $k_g = 10^{-24} \text{ m}/s$, $\text{TEOS} = 2.5 \times 10^{-4} \text{ mol}/L$). TEOS, tetraethylorthosilicate.

Table III. Comparison of Product Particle Size between Experiment and Simulation

Case	TEOS	Carrier gas		H ₂	O ₂	Air	Particle diameter (nm)	
	Concentration (mol/L)	1st tube (L/min)	2nd tube (L/min)	3rd tube (L/min)	4th tube (L/min)	5th tube (L/min)	Jang's experiment ¹²	Simulation
1	9.8×10^{-6}	1	10	6	15	40	11	15.6
2	2.5×10^{-4}	1	10	6	15	40	38	34.5
3	1.91×10^{-4}	1	10	6	15	20	26	30.8
4	9.8×10^{-6}	1	10 (replaced by air)	6	15	40	21	17.3
5	1.88×10^{-4}	1	10 (replaced by air)	6	15	40	32	30.9
6	1.38×10^{-4}	1	10 (replaced by air)	6	15	40	28	29.6
7	1.38×10^{-4}	1	10 (replaced by air)	6	5	50	18	Did not converge
8	1.38×10^{-4}	1	10	6	15	40	28	30.5
9	1.38×10^{-4}	1	10	4	15	42	28	35

TEOS, tetraethylorthosilicate.

gas flow rate was maintained the same by increasing the airflow rate in the fifth tube. As the oxygen flow rate decreased, the average particle diameter of the product decreased from 28 to 18 as shown in cases 6 and 7. For case 6, the simulation and the experimental result matched well. But in case 7, the simulation did not yield a converged result.

As the third change, the hydrogen flow rate in the third tube of the burner was decreased from 6 to 4 L/min at a constant total gas flow rate. The average particle diameter of the product remained nearly the same at 28 nm. The calculated average particle diameter increased somewhat from 30.5 to 35 nm.

The main purpose of this research was to simulate the synthesis process of silica nanoparticles from TEOS, which will be helpful in scaling-up of the process. Computed results for the scaled-up reactor are presented below.

When the scaled-up reactor was simulated, the number of cells was kept the same at 27 027. The entire domain was increased from 300 mm to 300×12.28 (3684 mm) in length and from 50 mm to 50×12.28 (614 mm) in radius. So far, this was the maximum size that yielded converged results. With the increase of the reactor size, the total feed linear rate had to be decreased in order to obtain a converged result in this work. For stable running, the flow rate through the first tube was 2 m/s of Ar plus TEOS; through the second, 0.055 m/s of Ar; through the third, 0.47 m/s of H₂; through the fourth, 0.87 m/s of O₂; and through the fifth, 1.83 m/s of air. The production rate increased approximately 560 times. k_n was set equal to 8 (#/s) and k_g was set equal to 10^{-24} (m/s). The energy convergence criterion was

changed to 10^{-5} , while others were kept the same. Figure 8 shows the results for the scaled-up processing in terms of product average particle size versus TEOS concentration. The average particle size was again based on specific surface area (m_3/m_2). When the TEOS concentration increased from 0.03 to 0.15 (mass fraction of TEOS in Ar plus TEOS inlet), the average particle diameter increased from 36 to 55 nm. These results need to be validated by future experiments.

Figure 9 shows the computed contours of average particle diameter in a scaled-up reactor with a concentration of TEOS of 6% in the feed stream. It is observed that the PSD is different from the experimental reactor. For the experimental reactor, the particles at the central part are quickly carried away by the feed gases; the particles remained briefly in the central region and remained longer in the region near the wall. Thus, particle size is smaller at the central part and larger near the wall. But for the scaled-up reactor, the inlet gas velocity was slower and the reactor size was larger. Thus, the particles spend more time near the center after being produced.

When more detailed experimental data become available, additional model validation can be performed, especially in terms of obtaining reliable values of the rate constants and with respect to the effects of process conditions as well as the spread in PSD.

IV. Concluding Remarks

A 2D CFD simulation was implemented to model the flame reaction process for silica nanopowder synthesis from TEOS. The fuel combustion process and silica particle formation and growth in the flame were simulated. The results for temperature, velocity profile, and PSD are reasonable. Various operating conditions such as different TEOS concentration and total gas flow rate and gas composition were tested. The combinations of assumed values of nucleation rate constant k_n ($\# \cdot s^{-1} \cdot m^3$) and growth rate constant k_g (m/s) that yield results that are consistent with experimental data have been identified. Finer particles are obtained with a lower precursor concentration. A higher oxygen concentration mixed with the precursor results in larger particles. The fact that the assumed value of k_g has a significant effect on the computed result indicates that the chemical reaction on the particle surface largely controls the growth rate and the mass transfer from the bulk gas is faster by comparison. It could be argued that the simulation could be improved further by using finer meshes and a more accurate nucleation and growth model, but this is very difficult for such a rapid chemical reaction process.

This work has shown that, by using CFD, details of combustion and particle formation and distribution inside the reactor can be obtained to a reasonable degree of satisfaction. To the best of the authors' knowledge, this is the first application of CFD to the flame synthesis of silica nanopowder. It is expected

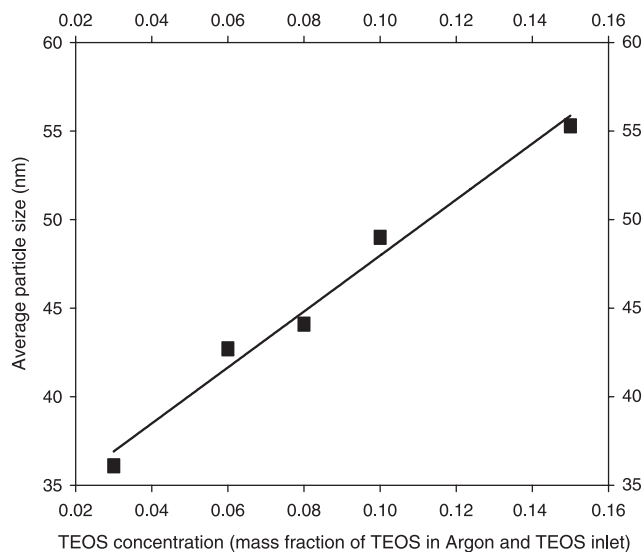


Fig. 8. Average particle diameter of product versus tetraethylorthosilicate (TEOS) concentration (scaled-up reactor).

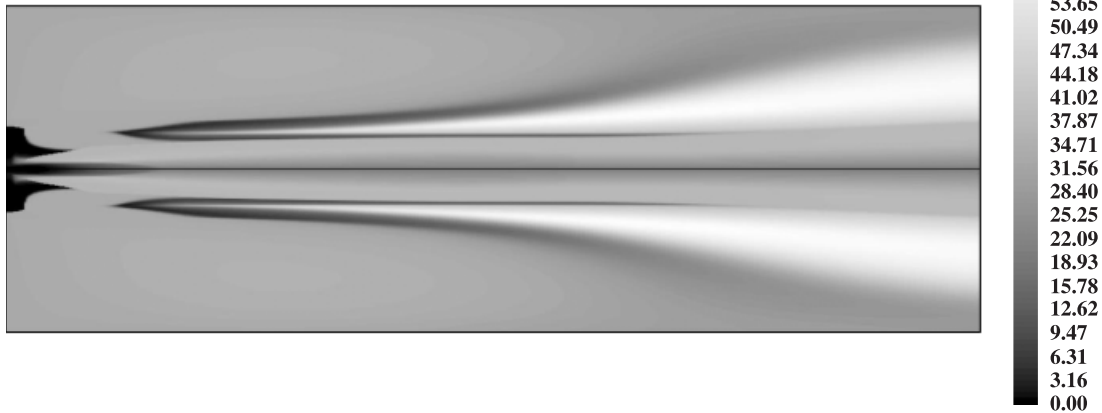


Fig. 9. Contours of average particle diameter (m) (scaled-up reactor, 6% TEOS). TEOS, tetraethylorthosilicate.

that this CFD simulation will be very useful in scaling up the flame reactor to an industrial scale.

Acknowledgments

The authors wish to thank Professor Philip J. Smith, Dr. Jennifer Spinti, and Mr. Eric Mortenson of the Department of Chemical Engineering, University of Utah, for their contribution with respect to CFD modeling during the early stage of this work. Thanks are also due to Miguel Olivas-Martinez for his assistance in the preparation of the paper. The license to the CFD computer code received from FLUENT Inc. is acknowledged with gratitude.

References

- ¹H. Gleiter, "Nanocrystalline Materials," *Prog. Mater. Sci.*, **33**, 223–315 (1989).
- ²R. W. Siegel, "Cluster-Assembled Nanophase Materials," *Annu. Rev. Mater. Sci.*, **21**, 559–78 (1991).
- ³R. W. Siegel, "Gas Evaporation and Electron Microscopical Observation of small Particles"; pp. 57–72 in *Nanophase Materials: Synthesis, Structure, and Properties*, Springer Series in Material Science, Vol. 260, NATO Science Series E: Applied Sciences, Edited by G. C. Hadjipanavis and R. W. Siegel Springer-Verlag, London, 1994.
- ⁴A. Gurav, T. Kodas, T. Pluym, and Y. Xiong, "Aerosol Processing of Materials," *Aerosol Sci. Technol.*, **19**, 411–52 (1993).
- ⁵H. K. Kammler, L. Mädler, and S. E. Pratsinis, "Flame Synthesis of Nanoparticles," *Chem. Eng. Technol.*, **24**, 583–96 (2001).
- ⁶G.D Ulrich and J. W. Riehl, "Aggregation and Growth of Submicron Oxide Particles in Flames," *J. Colloid Interface Sci.*, **87**, 257–65 (1982).
- ⁷W. Zhu and S. E. Pratsinis, "Synthesis of SiO₂ and SnO₂ Particles in Diffusion Flame Reactors," *A.I.Ch.E. J.*, **43**, 2657–64 (1997).
- ⁸J. Cho, J. Kim, and M. Choi, "An Experimental Study of Heat Transfer and Particle Deposition during the Outside Vapor Deposition Process," *Int. J. Heat Mass Transfer*, **41**, 435–45 (1998).
- ⁹S. H. Ehrman, S. K. Friedlander, and M. R. Zachariah, "Characteristics of SiO₂/TiO₂ Nanocomposite Particles Formed in a Premixed Flat Flame," *J. Aerosol Sci.*, **29**, 687–706 (1998).
- ¹⁰K. Okuyama, Y. Kousaka, H. Tohge, S. Yamamoto, J. J. Wu, R. C. Flagan, and J. H. Seinfeld, "Production of Ultrafine Metal Oxide Aerosol Particles by Thermal Decomposition of MetalAlkoxide Vapors," *A.I.Ch.E. J.*, **32**, 2010–9 (1986).
- ¹¹J. Smolik and P. Moravec, "Gas Phase Synthesis of Fine Silica Particles by Oxidation of Tetraethylorthosilicate Vapour," *J. Mater. Sci. Lett.*, **14**, 387–9 (1995).
- ¹²H. D. Jang, "Experimental Study of Synthesis of Silica Nanoparticles by a Bench-Scale Diffusion Flame Reactor," *Powder Technol.*, **119**, 102–8 (2001).
- ¹³H. D. Jang, "Generation of Silica Nanoparticles from Tetraethylorthosilicate (TEOS) Vapor in a Diffusion Flame," *Aerosol Sci. Technol.*, **30**, 477–88 (1999).
- ¹⁴H. D. Jang and H. S. Yoon, "Preparation of Ultrafine Silica Particles by Pyrolysis in the Gas Phase," *J. Korean Ind. Eng. Chem.*, **8**, 901–6 (1997).
- ¹⁵*FLUENT 6.1 User's Guide*. Fluent Inc., Lebanon, NH, 2003.
- ¹⁶A. D. Randolph and M. A. Larson, *Theory of Particulate Processes*, 2nd edition, Academic Press, New York, 1988.
- ¹⁷B. F. Magnussen and B. H. Hjertager, "On Mathematical Modeling of Turbulent Combustion with Special Emphasis on Soot Formation and Combustion"; pp. 719–29 in *Sixteenth Symposium (International) on Combustion*. The Combustion Institute, Cambridge, MA, 1976.
- ¹⁸K. S. Kim, J. K. Kim, and W. S. Kim, "Silica Particle Growth in Metastable Supersaturation Solution," *J. Mater. Res.*, **16**, 545–52 (2001).
- ¹⁹*FLUENT 6 Population Balance Model Manual*. Fluent Inc., Lebanon, NH, 2004.
- ²⁰B. Wan, "Computational Fluid Dynamics Simulation of Crystallization Process—Verification of Fluent's Population Balance Modeling"; Ph.D. Dissertation, University of Utah, Salt Lake City, Utah, 2005.
- ²¹D. L. Marchisio, A. A. Barresi, and R.O Fox, "Simulation of Turbulent Precipitation in a Semi-Batch Taylor-Couette Reactor Using CFD," *A.I.Ch.E. J.*, **47**, 664–76 (2001). □